A&A 597, A34 (2017)
DOI: 10.1051/0004-6361/201527775

Astronomy & Astrophysics

The Solar Twin Planet Search

V. Close-in, low-mass planet candidates and evidence of planet accretion in the solar twin HIP 68468

Jorge Meléndez[1], Megan Bedell[2], Jacob L. Bean[2], Iván Ramírez[3], Martin Asplund[4], Stefan Dreizler[5], Hong-Liang Yan[6], Jian-Rong Shi[6], Karin Lind[7], Sylvio Ferraz-Mello[1], Jhon Yana Galarza[1], Leonardo dos Santos[1], Lorenzo Spina[1], Marcelo Tucci Maia[1], Alan Alves-Brito[8], TalaWanda Monroe[9], and Luca Casagrande[4]

[1] Universidade de São Paulo, IAG, Departamento de Astronomia, Rua do Matão 1226, Cidade Universitária, 05508-900 São Paulo, SP, Brazil
e-mail: jorge.melendez@iag.usp.br
[2] University of Chicago, Department of Astronomy and Astrophysics, 5640 S. Ellis Ave, Chicago, IL 60637, USA
[3] University of Texas at Austin, McDonald Observatory and Department of Astronomy, TX 78712, USA
[4] The Australian National University, Research School of Astronomy and Astrophysics, Cotter Road, ACT 2611 Weston, Australia
[5] University of Göttingen, Institut für Astrophysik, 37073 Göttingen, Germany
[6] Key Laboratory of Optical Astronomy, National Astronomical Observatories, Chinese Academy of Sciences, 100012 Beijing, PR China
[7] Max Planck Institute for Astronomy, Königstuhl 17, 69117 Heidelberg, Germany
[8] Universidade Federal do Rio Grande do Sul, Instituto de Fisica, Av. Bento Goncalves 9500, 90040-060 Porto Alegre, RS, Brazil
[9] Space Telescope Science Institute, Baltimore, MD 21218, USA

Received 18 November 2015 / Accepted 2 September 2016

ABSTRACT

Context. More than two thousand exoplanets have been discovered to date. Of these, only a small fraction have been detected around solar twins, which are key stars because we can obtain accurate elemental abundances especially for them, which is crucial for studying the planet-star chemical connection with the highest precision.
Aims. We aim to use solar twins to characterise the relationship between planet architecture and stellar chemical composition.
Methods. We obtained high-precision (1 m s^{-1}) radial velocities with the HARPS spectrograph on the ESO 3.6 m telescope at La Silla Observatory and determined precise stellar elemental abundances (~0.01 dex) using spectra obtained with the MIKE spectrograph on the *Magellan* 6.5 m telescope.
Results. Our data indicate the presence of a planet with a minimum mass of 26 ± 4 Earth masses around the solar twin HIP 68468. The planet is more massive than Neptune (17 Earth masses), but unlike the distant Neptune in our solar system (30 AU), HIP 68468c is close-in, with a semi-major axis of 0.66 AU, similar to that of Venus. The data also suggest the presence of a super-Earth with a minimum mass of 2.9 ± 0.8 Earth masses at 0.03 AU; if the planet is confirmed, it will be the fifth least massive radial velocity planet candidate discovery to date and the first super-Earth around a solar twin. Both isochrones (5.9 ± 0.4 Gyr) and the abundance ratio [Y/Mg] (6.4 ± 0.8 Gyr) indicate an age of about 6 billion years. The star is enhanced in refractory elements when compared to the Sun, and the refractory enrichment is even stronger after corrections for Galactic chemical evolution. We determined a nonlocal thermodynamic equilibrium Li abundance of 1.52 ± 0.03 dex, which is four times higher than what would be expected for the age of HIP 68468. The older age is also supported by the low $\log(R'_{\rm HK})$ (–5.05) and low jitter (<1 m s^{-1}). Engulfment of a rocky planet of 6 Earth masses can explain the enhancement in both lithium and the refractory elements.
Conclusions. The super-Neptune planet candidate is too massive for in situ formation, and therefore its current location is most likely the result of planet migration that could also have driven other planets towards its host star, enhancing thus the abundance of lithium and refractory elements in HIP 68468. The intriguing evidence of planet accretion warrants further observations to verify the existence of the planets that are indicated by our data and to better constrain the nature of the planetary system around this unique star.

Key words. planetary systems – planets and satellites: detection – techniques: radial velocities – stars: abundances

1. Introduction

Soon after the discovery of the first exoplanets around solar-type stars (Mayor & Queloz 1995; Butler & Marcy 1996; Marcy & Butler 1996) a connection was noted between the metallicity of planet-host stars and the presence of close-in giant planets (Gonzalez 1997). Since then, our techniques to detect planets and to characterise stars have been substantially improved. It is now possible to achieve a precision of 1 m s^{-1} in radial velocity (RV), increasing our abilities to detect nearby small planets and distant large planets (e.g. Santos et al. 2004; Howard et al. 2011; Bedell et al. 2015). Additionally, a precision of 0.01 dex in chemical abundances has been achieved in solar twins (e.g. Bedell et al. 2014; Meléndez et al. 2014a; Ramírez et al. 2014; Tucci Maia et al. 2014; Nissen 2015). This is to be compared with a precision of ∼10 m s^{-1} for the first planet detections (Mayor & Queloz 1995; Butler & Marcy 1996; Marcy & Butler 1996) and errors of 0.08–0.09 dex in iron abundances of the first planet hosts (Gonzalez 1997).

Aiming to explore the planet-star connection more thoroughly, we are exploiting the synergy between precise chemical abundances that can be achieved in solar twins (0.01 dex) and precise planet characterisation that can be achieved with HARPS (1 m s^{-1}) through an on-going survey of planets around solar twins. Our sample was presented in Ramírez et al. (2014), where we determined stellar parameters ($T_{\rm eff}$, $\log g$, [Fe/H]), ages, masses, and stellar activity. Slightly improved ages and the [Y/Mg]-age relation were published in Tucci Maia et al. (2016). Our HARPS data have previously been used to obtain stringent constraints on planets around two important solar twins, 18 Sco, which is the brightest solar twin and is younger than the Sun (Meléndez et al. 2014a), and HIP 102152, an old solar twin with a low lithium content (Monroe et al. 2013). Our HARPS data were also used to study the rotation-age relation, showing that our Sun is a regular rotator (dos Santos et al. 2016).

The first planet detected in our HARPS survey is a Jupiter twin around the solar twin HIP 11915, a planet with about the mass of Jupiter and at about the same distance as the distance of Jupiter from the Sun (Bedell et al. 2015). Interestingly, the planet host star has the same volatile-to-refractory ratio as in the Sun, suggesting that in addition to being a Jupiter twin, it may host rocky planets, according to the hypothesis put forward by Meléndez et al. (2009).

In this paper we present the second and third planets discovered from our dedicated solar twin planet search. The evidence for the outer planet seems solid, but the inner planet is less well constrained. We discuss how the planet architecture may be related to the chemical abundance pattern.

2. Planet detection

2.1. Data

HIP 68468 was observed with the HARPS spectrograph (Mayor et al. 2003) on the ESO 3.6 m telescope at La Silla Observatory during 43 nights between 2012–2016 (the star was observed twice in two nights, resulting in 45 data points). These observations were carried out under our large program targeting 63 solar twin stars (program ID 188.C-0265). Each night's observation consisted of one 1300-s exposure for this V = 9.4 star. This exposure time is long enough to average out p-mode stellar oscillations typical of solar-like stars, and to achieve a photon-limited precision of 1 m s^{-1} in typical observing conditions. On two of the observing nights, two 1300-s exposures were taken with a two-hour time gap between them. In total, we obtained 45 RV measurements for the star.

All HARPS data were processed with version 3.8 of the dedicated HARPS pipeline, which determines radial velocities through a cross-correlation technique using a G2 binary mask. Uncertainties on the RVs came from the pipeline estimation, which accounts for photon noise in the cross-correlation. An additional 1 m s^{-1} was added in quadrature to account for the instrumental noise floor (Dumusque et al. 2011). The Ca II H&K spectral lines were measured by us, and the resulting $S_{\rm HK}$ activity indices were converted into the standard Mount Wilson $\log(R'_{\rm HK})$ index using the relation derived by Lovis et al. (2011).

The HARPS instrument underwent an upgrade in June 2015 that included the installation of new fibers and instrumental refocusing. This upgrade altered the instrumental profile and introduced offsets in the measured RVs relative to the pre-upgrade RV zero point. We used the data for a set of ten stars in our program with relatively constant pre-upgrade RV time series (RMS < 2 m s^{-1}) to characterise the offset. Although this offset is expected to have a dependence on stellar type, all stars in our program are solar twins and should therefore share the same offset. We find an offset of 15.4 ± 0.2 m s^{-1} among the constant solar twin sample. This value agrees with those obtained by the HARPS team using RV standard stars (Lo Curto et al. 2015). To properly account for the effect of the upgrade and its uncertainty, we include the RV offset as a free parameter in the model as described below.

All HARPS RVs and relevant activity indices are given in Table B.2.

2.2. Analysis and results

We identified candidate planet periods using a generalised Lomb-Scargle periodogram (Zechmeister & Kürster 2009). For this initial analysis, we subtracted a 15.4 m s^{-1} offset from the data taken after the HARPS upgrade. Leaving aside the 1.0 and 0.5-day peaks that commonly arise from a nightly sampling cadence, the strongest periodicity in the data is at 194 days (Fig. 1). To calculate its false-alarm probability (FAP), or the probability that such a high-power peak could appear through random noise, we used a bootstrap Monte Carlo technique. The data were bootstrap sampled for 5000 trials, with the power of the highest peak recorded for each trial. The 90th and 99th percentiles of the resulting power distribution can be used as approximate 10% and 1% FAP thresholds. For the 194 day peak, we find that only 0.8% of the trials yielded a peak of equal or greater height by chance. The analytic FAP, using the formulation of Zechmeister & Kürster (2009), is even lower at 0.2%. Although 194 days is somewhat close to half a year and the associated window function peak at 171 days, the phase coverage of the signal is nonetheless sufficient to reliably fit a Keplerian. No combination of significant periodicities from the window function and the data would feasibly combine to produce an alias peak at a 194-day period (Dawson & Fabrycky 2010).

We modelled and removed the 194 day signal using a least-squares algorithm to simultaneously fit the Keplerian orbital parameters and the RV offset introduced by the HARPS upgrade ($\delta_{\rm inst}$). The periodogram of the residuals to this fit showed a peak at 1.84 days with a bootstrap FAP of 2%. Adding a Keplerian with a 1.84-day period to the least-squares model fit yielded a two-planet solution which substantially reduced the residuals of the one-planet fit. Further observations need to be gathered to better constrain the inner planet, as an alternative solution with a period of ∼2.3 days seems to exist.

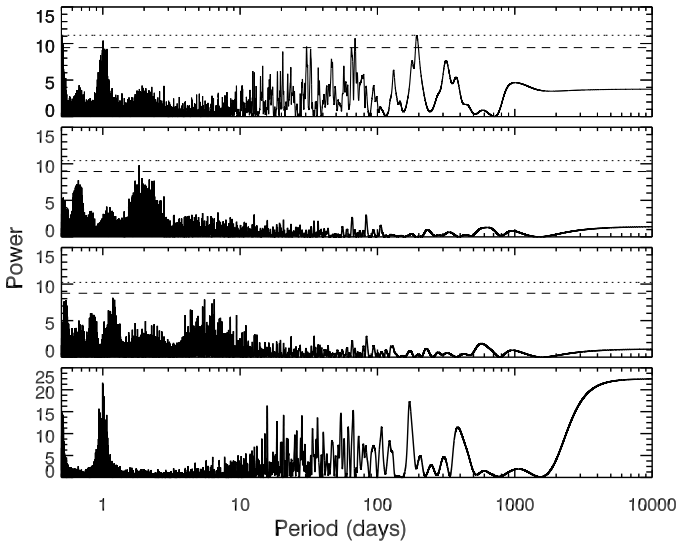

Fig. 1. Generalised Lomb Scargle (GLS) periodograms to determine the frequencies of planet candidates. *Top panel* is a periodogram of the original data with instrumental upgrade offset removed. *Middle panels* are periodograms of the residuals to a 194-day Keplerian fit (*upper middle*) and a two-planet fit (*lower middle*). The horizontal lines represent false-alarm probability levels of 10% (dashed) and 1% (dotted), as calculated from a bootstrap Monte Carlo method. Also included for comparison is the window function of the sampling (*bottom panel*).

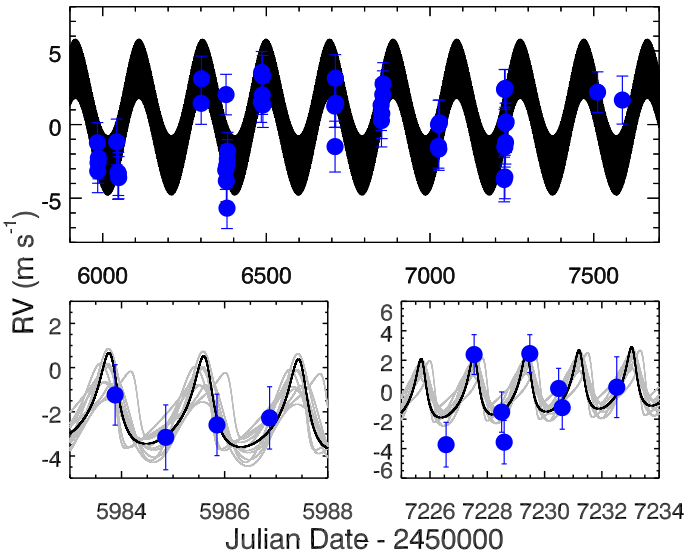

Fig. 2. Full time series of RV data (blue) and two-planet best-fit model. The *two lower panels* show zoomed-in subsets of the time series. The black line is the best-fit model from a least-squares fit. The grey lines are models randomly drawn from the one-sigma range of best steps in the MCMC analysis. As illustrated by the grey models, the eccentricity of the inner planet is not well constrained.

After removing both 194-day and 1.84-day signals, no significant peaks remained in the residuals periodogram (Fig. 1).

We ran a Markov chain Monte Carlo (MCMC) analysis using the specific implementation of Bedell et al. (2015) to obtain final confidence intervals on the two planet candidate orbits, properly marginalising over all uncertain parameters. Our model consisted of two Keplerian signals, a constant RV offset C relative to the instrumental zero point, an instrumental offset $\delta_{\rm inst}$ for post-HARPS upgrade RVs, and a jitter term $\sigma_{\rm J}$. The Keplerian signal was parameterised as (P, K, e, $\omega + M_0$, $\omega - M_0$), where P is the orbital period, K is the RV semi-amplitude, e is eccentricity, ω is the argument of periastron, and M_0 is the mean anomaly at a reference date set by the first RV measurement in the time series. All of the fit parameters were given uniform priors except for P and K, which were sampled in log-space with a log-uniform prior, and $\delta_{\rm inst}$, which was given a Gaussian prior with the mean and uncertainty as given in Sect. 2.1. After the MCMC run concluded, the chains were examined for non-convergence using the Gelman-Rubin statistic and any chains that had become stuck in a low-likelihood region of parameter space were removed from the posterior (Gelman & Rubin 1992).

The resulting constraints on the two-planet fit are presented in Table 1. Owing to strong correlations between the parameters and poorly constrained phases, taking the median values from each parameter posterior does not result in a good fit. We quote the best-fit values from the maximum likelihood fit and MCMC median values in Table 1. The quoted errors are the one-sigma range, percentile-wise, from the MCMC posteriors. The orbital solutions shown in Figs. 2 and 3 use the best-fit parameters.

The final solution from the MCMC corresponds to a 2.9 ± 0.8 Earth mass planet with an orbital period of 1.8374 ± 0.0003 days and a 26 ± 4 Earth mass planet with an orbital period of 194 ± 2 days. Both eccentricities are consistent with zero within 2σ. The jitter term is low (consistent with zero), indicating that HIP 68468 is a relatively quiet star without much activity.

2.3. Model comparison

Periodograms are a useful tool for identifying signal periods of interest, but the periodogram FAP is not the most robust tool available to assess the reality of signals found. We ran multiple MCMCs to fit alternative models to the data. All models include the instrumental offset factors and a jitter term, but vary in the number of Keplerian signals included. We compared the models using the Bayesian information criterion (BIC, Kass & Raftery 1995), calculated from the highest likelihoods achieved in the MCMCs for each model. The results indicate that the two-planet model including a 1.84-day super-Earth has the smallest BIC and is therefore the most likely solution of those tested (see Table 2). We also compared the best-fit solutions for each model as determined by a least-squares algorithm with similar results.

Evidence from the BIC and $\chi^2_{\rm red}$ strongly supports the presence of the outer planet: the Δ BIC is large at 11.5, and an F-test comparing the one-planet model to the no-planet model gives a probability of about 10^{-4} against the planet presence. Inclusion of the super-Earth signal improved the fit further, reducing the $\chi^2_{\rm red}$ from 1.6 to 1.0 and bringing the RMS down from 1.7 to 1.3 m s^{-1}. An F-test comparison using the best-fit chi-squared statistics gives a probability of 7×10^{-4} that the inclusion of the second planet is unwarranted.

2.4. Stellar activity indicators

Although HIP 68468 is a quiet star with a low $\log(R'_{\rm HK})$ value (averaging –5.05 in the HARPS spectra), we nevertheless examined the data for signs that stellar activity might be inducing a false RV signal. No statistically significant trends were found between RV and $\log(R'_{\rm HK})$ or bisector inverse span (BIS). A marginally significant correlation was found between RV and the full width at half maximum (FWHM) of the cross-correlation function, with a p-value of 1.4% from bootstrap resampling. Subtracting this trend from the RV data does not have a noticeable effect on the shape of the periodogram; a peak around

Table 1. Best-fit parameters and uncertainties for HIP68468 b and c.

Parameter		HIP 68468 b		HIP 68468 c	
		Best-fit value	MCMC posterior	Best-fit value	MCMC Posterior
P	[days]	1.8372	1.8374 ± 0.0003	194	194 ± 2
K	[m s^{-1}]	2.0	1.5 ± 0.5	3.3	2.9 ± 0.5
e		0.41	$0.24^{+0.24}_{-0.17}$	0.04	$0.11^{+0.14}_{-0.08}$
$\omega + M_0$	[rad]	3.0	2.7 ± 1.7	0.0	$3.7^{+1.9}_{-2.5}$
$\omega - M_0$	[rad]	2.5	$2.4^{+0.5}_{-0.4}$	1.0	$1.0^{+0.2}_{-0.3}$
$m_p \sin(i)$	[M_{Earth}]	3.5	2.9 ± 0.8	30	26 ± 4
a[1]	[AU]	0.029743	0.029744 ± 0.000003	0.665	0.664 ± 0.004
C	[m s^{-1}]	1257.2	$1256.2^{+1.1}_{-0.8}$		
δ_{inst}	[m s^{-1}]	15.4	15.5 ± 0.2		
σ_J	[m s^{-1}]		$0.4^{+0.4}_{-0.3}$		
RMS	[m s^{-1}]	1.3			

Notes. [(1)] Using host star mass of 1.05 $M_\odot$ (see text); error estimates do not include uncertainty on the stellar mass.

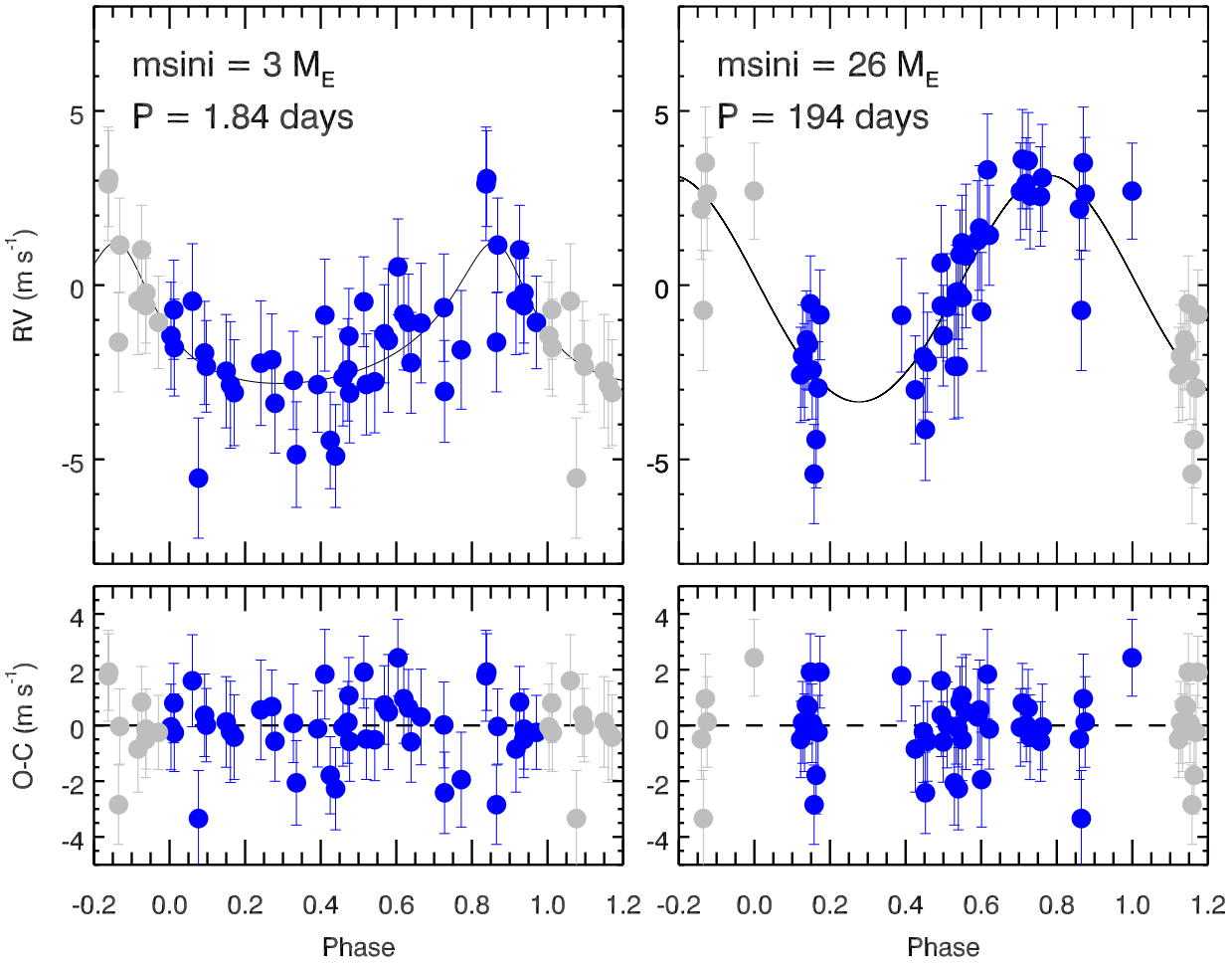

Fig. 3. Phase-folded RV data for the two Keplerian signals. The *upper panels* show the RV data with the other planet and offsets removed. Our final MCMC solution is overplotted, with residuals in *the lower panels*. Grey points are duplicated observations plotted for clarity.

190 days still stands out, although the significances of all peaks are reduced.

The periodogram of the FWHM shows a peak at 41 days, which may be a signature of the rotation period (Fig. 4). We were unable to fit and subtract any quasi-periodic 41-day activity signals from the data as suggested in Dumusque et al. (2011), for example. This could be due to the limitations of the time-series sampling in resolving any evolving stellar activity. We instead

treated the relationship between activity indicator and activity-induced RV shift as a linear trend with an unknown slope, which should be accurate as a first-order approximation (Dumusque et al. 2014).

We ran the MCMC algorithm with models incorporating a linear FWHM correlation in addition to the Keplerian signal(s). Because the FWHM measurement suffered the same unknown offset effect as the RVs after the HARPS upgrade, we accounted for this in a similar way by adding an additional $\delta_{\rm inst,FWHM}$ term to the model with a strong prior based on the average FWHM offset among our constant stars of 15.6 ± 0.4 m s^{-1}.

Regardless of initial conditions, the strength of the FWHM correlation term consistently went to a low value (0.13 ± 0.05). All of the orbital parameters for the two-planet solution remained well within 1σ of the values given in Table 1. We therefore conclude that any stellar activity traced by the FWHM is most likely independent of the Keplerian signals in the data. We chose not to include the FWHM correlation in the final fit presented based on the weak evidence for its addition to the model: a marginally higher BIC by 1 compared to the two-planet model, and an F-test probability of 8% that the addition of a correlation term is unwarranted. We note, however, that the two-planet model remains the best fit regardless of whether or not an FWHM correlation is included (Table 2).

2.5. Orbital eccentricities

Both the MCMC and least-squares fitting yield non-zero eccentricities for the two Keplerian orbits. However, as a positive definite parameter, eccentricity is prone to overestimation when an orbit is truly circular (Zakamska et al. 2011). We present the posterior distributions of several key orbital parameters, including eccentricity, in Fig. 5. From the posteriors, it is clear that the mode of the eccentricity distribution (recommended as the least biased estimator by Zakamska et al. 2011) is within 1σ of zero for the two planet candidates. Nevertheless, we chose not to fix either eccentricity to zero in the MCMC analysis because the uncertainty on eccentricity should be marginalised over when making an estimate of the errors on all parameters.

The eccentricity found for the innermost planet (HIP 68468b) is remarkably high, albeit as discussed above, within the uncertainties $e = 0$. If the high eccentricity is confirmed with further RV observations, it would be a short-lived phenomenon, as the orbit should be circularised on a timescale $\ll$1 Gyr. The exact timescale for tidal circularisation would be better defined once a more precise eccentricity is available and when a measurement of the planet radius is made through transit observations, so that we can estimate the planet composition. We have recently obtained observing time with the *Spitzer* Space Telescope to attempt the transit detection of HIP 68468b.

3. Fundamental parameters and abundance analysis

3.1. Data and measurements

The spectra of HIP 68468 and the Sun (reflected light from the asteroid Vesta) were taken using the MIKE spectrograph (Bernstein et al. 2003) at the 6.5 m *Clay Magellan* telescope. The data were obtained with $R = 65\,000$ in the red side (500–1000 nm) and $R = 83\,000$ in the blue side (320–500 nm). The spectra have a signal-to-noise ratio (S/N) $\approx$ 400 per pixel at 600 nm. The

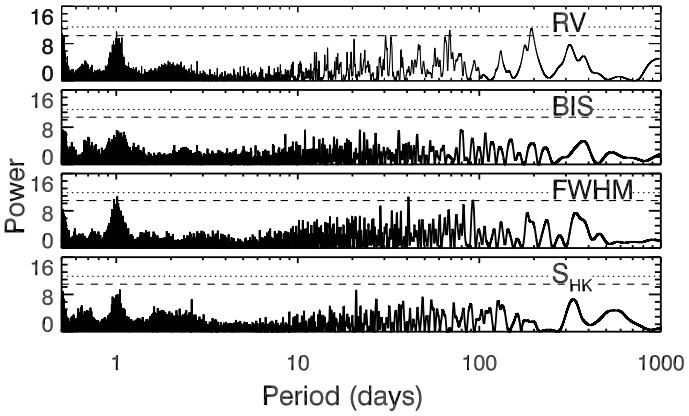

Fig. 4. GLS periodograms of the RV data and various activity indicators for comparison. Horizontal lines correspond to false-alarm probabilities of 10% (dashed) and 1% (dotted), as calculated from bootstrap Monte Carlo resampling.

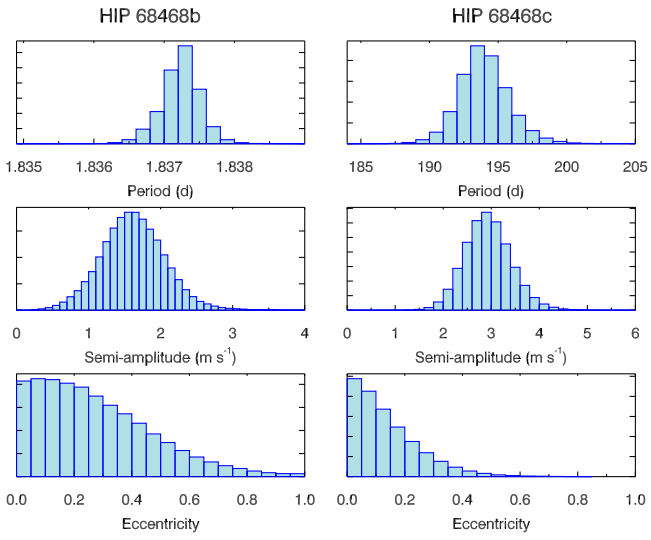

Fig. 5. Posterior distributions of orbital period, radial velocity semi-amplitude, and eccentricity for the two planet candidates.

data were reduced using the CarnegiePython MIKE pipeline[1], and further processing (Doppler correction and continuum normalisation) was performed as described in Ramírez et al. (2014). The MIKE data were employed to perform the equivalent width (EW) measurements used to determine stellar parameters and chemical abundances, and for spectral synthesis to determine $v \sin i$ and the lithium content.

The HARPS spectra described in Sect. 2.1 have a more limited wavelength coverage (380–690 nm) than the MIKE spectra, but they have a higher resolution ($R = 120\,000$), hence they were used to verify through spectral synthesis both $v \sin i$ and the Li abundance. The combined HARPS spectrum of HIP 68468 has $S/N \sim 750$ at 600 nm.

The EW were measured comparing line-by-line the spectrum of HIP 68468 to the Sun in a 6 Å window, to help determine the continuum and to choose the part of the line profile that was used to fit a Gaussian profile. After the first set of measurements was obtained, 2σ outliers were identified from the differential analysis and their EW were verified. The remeasured EW were

[1] http://code.obs.carnegiescience.edu/mike

Table 2. Comparison of RV models.

	BIC	$\chi^2_{\rm red}$	RMS [m s^{-1}]
No planets	217.8	2.9	2.4
No planets + FWHM correlation	222.8	2.6	2.3
194-d Keplerian	206.3	1.6	1.7
194-d Keplerian + FWHM correlation	211.0	1.6	1.7
194-d & 1.84-d Keplerians	199.0	1.0	1.3
194-d & 1.84-d Keplerians + FWHM correlation	200.2	0.9	1.2

kept, unless there was a problem, such as a contamination by a telluric line or a defect in one of the spectra.

3.2. Stellar parameters

The stellar parameters for our solar twin planet search sample were published in Ramírez et al. (2014). Only three of the sample stars had revised stellar parameters based on the [Y/Mg] ratio, which can be used as a proxy for stellar ages (Nissen 2015). The comparison between our isochrone ages (Ramírez et al. 2014) and the [Y/Mg] ratio (Tucci Maia et al. 2016) shows that [Y/Mg] ages can be determined to better than 0.9 Gyr. As the isochrone age of HIP 68468 determined in Ramírez et al. (2014) was off by 1.2 Gyr relative to the age obtained from the [Y/Mg] ratio, and because the age of this star plays an important role in our interpretation, a reanalysis of HIP 68468 was performed as described below.

We adopted the same line list as in Ramírez et al. (2014). The EW measurements were used to obtain elemental abundances with the *abfind* driver of MOOG (Sneden 1973), using Kurucz model atmospheres (Castelli & Kurucz 2004). Then, line-by-line differential abundances were obtained.

The stellar parameters ($T_{\rm eff}$, $\log g$, [Fe/H], $v_{\rm t}$) of HIP 68468 were determined by imposing a differential spectroscopic equilibrium of iron lines relative to the Sun (e.g. Meléndez et al. 2014a), using as initial parameters the values given in Ramírez et al. (2014). The solar values were kept fixed at ($T_{\rm eff}$, $\log g$, $v_{\rm t}$) = (5777 K, 4.44 dex, 1.0 km s^{-1}). Our solution for HIP 68468 gives consistent differential abundances for neutral and ionised species of different elements, and also for atomic and molecular lines, as discussed in more detail in the next section.

The errors in the stellar parameters were obtained from the uncertainties in the slope of the fits of the differential abundances versus excitation potential and reduced EW, and the errors in the differential ionisation equilibrium (based on the observational uncertainties in the differential abundances of FeI and FeII), and including also the degeneracy among the stellar parameters.

The resulting stellar parameters are $T_{\rm eff}$ = 5857 ± 8 K, $\log g$ = 4.32 ± 0.02, [Fe/H] = 0.065 ± 0.007, $v_{\rm t}$ = 1.14 ± 0.01 km s^{-1}, which agree well with the previous estimate (5845 ± 6 K, 4.37 ± 0.02 dex, 0.054 ± 0.005 dex, 1.13 ± 0.01 km s^{-1}) by Ramírez et al. (2014). The most important difference is seen in the $\log g$ value, which is reduced by 0.05 dex. This has a non-negligible effect on the derived age of the star (0.7 Gyr, see below). HIP 68468 is one of the most distant stars in our solar twin planet search sample, which prevents us from using its Hipparcos parallax to better constrain this important parameter. The Hipparcos parallax of HIP 68468 has an error greater than 10% and the trigonometric $\log g$ value that we derive using that parallax is fully consistent with both the old and new spectroscopic parallaxes within the errors.

The mass and age of HIP 68468 were determined using Y^2 isochrones (Demarque et al. 2004), as described in Meléndez et al. (2012) and Ramírez et al. (2013). With our stellar parameters and their uncertainties, we used probability distribution functions to infer a mass M = 1.05 ± 0.01 $M_\odot$ and age of 5.9 ± 0.4 Gyr (Fig. 6), which are similar to those reported by Ramírez et al. (2014), 1.04 ± 0.01 $M_\odot$ and $5.2^{+0.4}_{-0.5}$ Gyr.

Recently, Nissen (2015) has shown a tight correlation between [Y/Mg] and age that is corroborated by our own study (Tucci Maia et al. 2016). HIP 68468 has [Y/Mg] = −0.087 ± 0.017 dex, implying in an age of 6.4 ± 0.8 Gyr (using the relation by Tucci Maia et al. 2016). This age agrees well with our isochrone age (5.9 ± 0.4 Gyr). Thus, both isochrones and [Y/Mg] suggest that HIP 68468 has an age of about 6 Gyr.

The post-solar age of HIP 68468 is further supported by its low activity level. The HARPS spectra give an activity index $\log(R'_{\rm HK})$ = –5.05 ± 0.02, where the error comes from the standard deviation across all spectra in the time series. Using the relationship derived by Mamajek & Hillenbrand (2008) and a stellar $(B-V)$ of 0.68 (Høg et al. 2000), this translates into an expected age of 7.6 ± 0.4 Gyr, but we note that the activity-age relation is not well defined above 3 Gyr (Ramírez et al. 2014), hence the above error bar is underestimated.

The projected rotational velocity of HIP 68468 was estimated through spectral synthesis by dos Santos et al. (2016), taking into account both the instrumental ($\Delta\lambda = \lambda/R$) and macroturbulent broadening (using a radial-tangential macroturbulence profile; Gray 2005).

We note that if the macroturbulence ($V_{\rm macro}$) is estimated from $V_{\rm macro} - T_{\rm eff}$ relations (e.g., Meléndez et al. 2012), then HIP 68468 seems to be rotating faster than it should for its age, when compared to other solar twins analysed with the same method. However, even for main-sequence stars the luminosity effect on macroturbulence is not negligible (Doyle et al. 2014). dos Santos et al. (2016) provided a new macroturbulence calibration that takes the $T_{\rm eff}$ and $\log g$ dependence into account. This gives a projected rotation velocity for HIP 68468 of $v \sin i$ = 1.92 ± 0.13 km s^{-1} (dos Santos et al. 2016), which agrees within the errors with the rotation velocity predicted by the $v_{\rm rot}$-age relation by dos Santos et al. (2016) at HIP 68468's age (5.9 Gyr), $v_{\rm rot}$ = 1.86 km s^{-1}.

3.3. Stellar abundances

The chemical composition was determined using the line list by Meléndez et al. (2014a) for atomic lines. To verify the carbon abundances obtained from permitted atomic lines, we also obtained differential abundances using the molecules CH and C_2, adopting the molecular data given in Asplund et al. (2005).

For the elements V, Mn, Co and Cu, we took hyperfine structure (HFS) into account. The differential HFS correc-

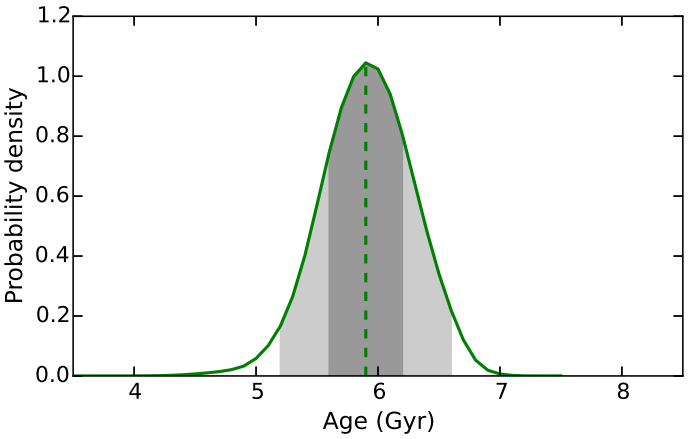

Fig. 6. Age probability distribution of HIP 68468. The dark and light areas correspond to 1σ and 2σ confidence.

tions are small because of the similarity between HIP 68468 and the Sun. Differential non-local thermodynamical equilibrium (NLTE) corrections in solar twins are also usually small, as shown in our previous works (Meléndez et al. 2012, 2014a; Monroe et al. 2013). Still, we performed NLTE corrections for Li (Lind et al. 2009), O (Ramírez et al. 2007), Na (Lind et al. 2011), Mg, Ca (Lind et al., in prep., see Appendix A), and Cu (Shi et al. 2014; Yan et al. 2015). The differential NLTE corrections are small for most elements, amounting to −0.004, −0.006, −0.004 and 0.000 dex for Na, Mg, Ca, and Cu, respectively. Only for the oxygen triplet was the differential NLTE effect strong, amounting to −0.028 dex.

The final differential abundances, after taking into account HFS and NLTE effects, are listed in Table B.1, where LTE abundances are also shown for completeness. These abundances are plotted as a function of condensation temperature in Fig. 7. The upper panel shows the excellent agreement between neutral and ionised species (shown by triangles) for the elements Cr, Fe (forced by the analysis), Ti, and Sc. The carbon abundance obtained from neutral carbon atomic lines and those obtained from CH and C_2 lines (both shown by triangles in Fig. 7) also agree well. This consistency supports our determination of stellar parameters, as lines from different species have different dependence on the stellar parameters.

The abundance errors are reported in Table B.1 and are based on the measurement errors (standard error) and systematic errors due to the uncertainties in the stellar parameters. The total errors are on average 0.012 dex. This is similar to the 0.01 dex errors achieved with high-quality spectra of stellar twins (e.g. Meléndez et al. 2012; Monroe et al. 2013; Bedell et al. 2014; Ramírez et al. 2015; Teske et al. 2016).

The lithium feature is clearly visible and deeper than in the Sun, so that a reliable lithium abundance can be estimated. The Li content was obtained using spectral synthesis in LTE, including blends by atomic and molecular (CN, C_2) lines, employing the line list of Meléndez et al. (2012). Using the MIKE spectrum, we obtain an LTE lithium abundance of $A(\mathrm{Li}) = 1.49 \pm 0.05$, and our HARPS spectrum results in $A(\mathrm{Li}) = 1.47 \pm 0.04$ (Fig. 8). We adopted an LTE abundance of $A(\mathrm{Li}) = 1.48 \pm 0.03$ (weighted average), and using the NLTE corrections mentioned above (Lind et al. 2009), $A(\mathrm{Li}) = 1.52 \pm 0.03$ was obtained.

The Li abundance in HIP 68468 (1.52 ± 0.03 dex) is much higher (four times; 0.6 dex) than expected for its age (Monroe et al. 2013; Meléndez et al. 2014b; Carlos et al. 2016). This is shown in Fig. 9, where HIP 68468 is compared with solar twins

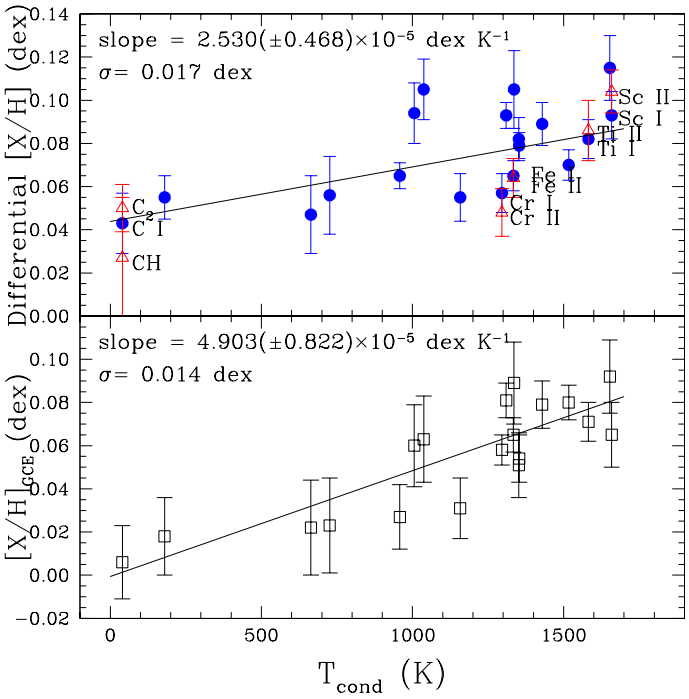

Fig. 7. *Upper panel*: observed abundance pattern of HIP 68468 versus condensation temperature before GCE corrections. The solid line is a fit taking into account the total error bars. It has a significance of 5.4σ, and the element-to-element scatter from the fit is 0.017 dex, which is larger than the average error bar (0.012 dex). *Lower panel*: abundance pattern after GCE corrections to the solar age. The error bars also include the error of the GCE corrections, and has an average of 0.014 dex. The correlation with condensation temperature is now stronger and more significant (6.0σ), and the element-to-element scatter about the fit (0.014 dex) is in perfect agreement with the average error bar.

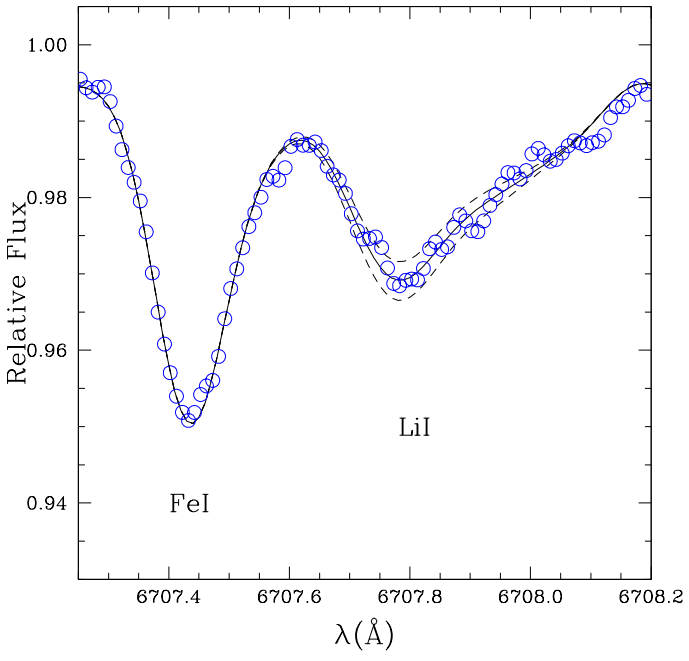

Fig. 8. Lithium feature in the HARPS spectrum of HIP 68468 (open circles) and synthetic spectrum with an LTE lithium abundance of 1.47 dex (solid line), corresponding to an NLTE abundance of $A(\mathrm{Li}) = 1.51$ dex. A variation of ±0.04 dex in the Li abundance is shown by dashed lines. The variations seen in the line profile are mostly consistent with the noise in this region ($S/N \sim 500$), but could also be due to distinct convective line shifts between different species.

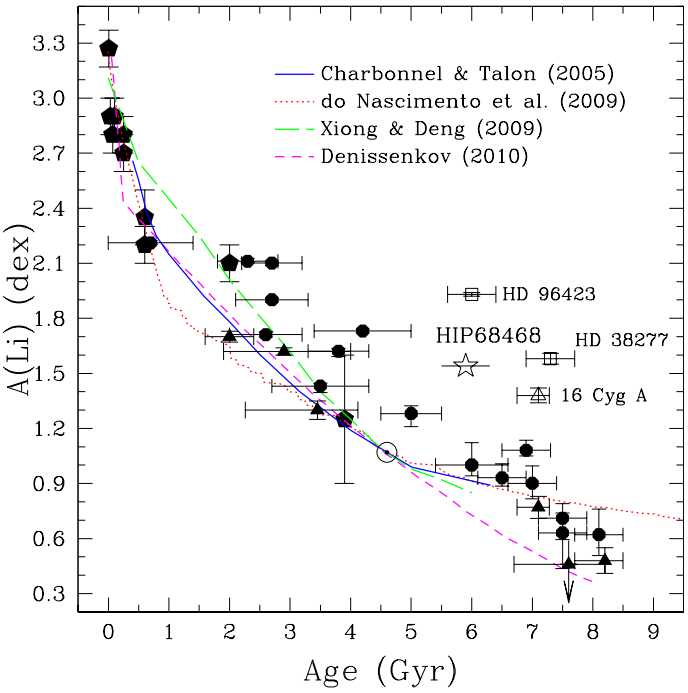

Fig. 9. Lithium abundances versus age. The Li abundance of HIP 68468 was determined in this work. For the field solar twins (circles, triangles, squares) we used the values given in our previous works (Carlos et al. 2016; Galarza et al. 2016a; Meléndez et al. 2012, 2014a,b; Monroe et al. 2013; Ramírez et al. 2011), and for the solar twins in open clusters (pentagons) we adopted the values given in Baumann et al. (2010) and Castro et al. (2011), as described in the text. We also show non-standard models of lithium depletion (Charbonnel & Talon 2005; do Nascimento et al. 2009; Xiong & Deng 2009; Denissenkov 2010), normalised to the Sun.

analysed in our previous works (Ramírez et al. 2011; Meléndez et al. 2012, 2014a,b; Monroe et al. 2013; Carlos et al. 2016; Galarza et al. 2016a) and to solar twins in open clusters using data by Baumann et al. (2010), except for the cluster M 67, where the Li abundances are from the updated results using spectrum synthesis by Castro et al. (2011). The solar twins in M 67 were selected from their list of solar analogs (Table 1), considering $T_{\rm eff} = T_{\rm eff\odot} \pm 100$ K and $L = 1.0 \pm 0.1\ L_{\odot}$. The mean LTE Li abundance in M 67 solar twins is 1.25 ($\sigma = 0.35$ dex), with the scatter being due partly to the uncertain values (some are only upper limits) given in Castro et al. (2011). Nevertheless, the mean Li abundance is similar to the LTE Li abundance (1.26 dex) of the only solar twin (M 67-1194) analysed at high precision in this cluster (Önehag et al. 2011). Although there might be some slight variations in Li as a result of slightly different masses and metallicities, contributing thus to the observed scatter in the Li-age correlation, the variations for our small range in mass and metallicity are small (Baumann et al. 2010; Carlos et al. 2016), hence our comparison between HIP 68468 and other solar twins is valid.

The decay of lithium with age is supported by stellar evolution models including transport processes beyond merely the mixing length convection (Charbonnel & Talon 2005; do Nascimento et al. 2009; Xiong & Deng 2009; Denissenkov 2010), as shown in Fig. 9. Lithium is depleted and not produced in stars like the Sun, therefore the enhanced lithium abundance of HIP 68468 is probably due to external pollution. Carlos et al. (2016) have also recently identified two stars with enhanced lithium abundances (open squares in Fig. 9) and suggested that they may have been polluted in lithium by planet ingestion, which might also be the case of 16 Cyg A (open triangle in Fig. 9).

There are four stars with enhanced lithium abundances in the sample of 27 thin-disc solar twins shown in Fig. 9 (HIP 68468, HD 38277, HD 96423, 16 Cyg A). Adopting a binomial distribution (see e.g. Sect. 4.4 in Ramírez et al. 2012), the above numbers suggest that $15 \pm 2\%$ of Sun-like stars may have visible signatures of planet ingestion.

4. Discussion

The presence of a giant planet and a small super-Earth in close-in orbits gives us the opportunity to study how this configuration might be related to the chemical abundance pattern in HIP 68468.

In Fig. 7 (upper panel) we show that the abundance pattern of HIP 68468 (relative to the Sun) has a correlation with condensation temperature ($T_{\rm cond}$). The fit of [X/H] vs. $T_{\rm cond}$ is represented by a solid line. This correlation is well defined, with a significance higher than 5σ. The element-to-element scatter about the fit is 0.017 dex, which is higher than the average abundance error of 0.012 dex, but this is likely due to the scatter introduced by galactic chemical evolution (GCE), as described in recent works (Nissen 2015; Spina et al. 2016).

Employing the relations between age and stellar abundances obtained by Spina et al. (2016) using solar twins, we can correct for GCE effects, which enables a more proper comparison to the Sun, which is $\Delta_{\rm age} = 1.3$ Gyr younger than HIP 68468. We subtracted the GCE effects corresponding to this age interval, resulting in abundance ratios corrected to the Sun's age,

$$[{\rm X/H}]_{\rm GCE} = [{\rm X/H}] - {\rm slope} * \Delta_{\rm age}, \quad (1)$$

where the slope of the GCE corrections for the different chemical elements is taken from Table 3 of Spina et al. (2016).

The corrected abundance ratios are shown in the bottom panel of Fig. 7. In this plot the elements with different species were weight averaged, using as weights the inverse square of their error bars. The error bars now also include the error on the GCE corrections, which are due to the error on the slope of the abundance variations with age (Spina et al. 2016) and also considering the error on the age of HIP 68468. As a result, the typical error bar increased from 0.012 dex to 0.014 dex. The $[{\rm X/H}]_{\rm GCE}$ ratios now show a higher refractory enhancement and a stronger correlation with $T_{\rm cond}$, at the level of 6σ. The scatter about the fit is now 0.014 dex, identical to the typical error bar in the $[{\rm X/H}]_{\rm GCE}$ ratios.

The close-in giant planet suggests migration from an outer to the inner ($\leq$1 AU) region. This migration could have driven inner planets towards its host star, leading to planet engulfment events and to changes in the abundance pattern of the convection zone (Sandquist et al. 2002). The super-Earth that we seem to have detected may also follow this fate, as it is located at only 0.03 AU from HIP 68468. If HIP 68468b survives, it surely would be destroyed when HIP 68468 evolves from the main sequence.

Past planet accretion effects could be reflected in enhanced abundances of the refractory elements, and also an increase in the lithium abundance. As lithium is affected by stellar depletion by more than a factor of 100 at the solar age (e.g. Asplund et al. 2009; Monroe et al. 2013), it is relatively easy to increase the low photospheric Li content by planet accretion. As shown by Sandquist et al. (2002), in a planet migration scenario and further accretion to its host star, the planet material would be mixed in

the stellar convection zone and would modify the surface abundances, in particular for Li (see also Tognelli et al. 2016; Murray & Chaboyer 2002; Montalbán & Rebolo 2002).

Using the abundance pattern of the Earth and meteorites, we can estimate the rocky mass needed to increase the refractory elements to the levels observed in HIP 68468, following the procedure outlined in Chambers (2010) and Galarza et al. (2016b). We estimated a convective mass of 0.018 $M_{\odot}$, using the tracks by Siess et al. (2000). In Fig. 10, we show the $[X/H]_{GCE}$ ratios by red circles and the effect due to the accretion of 6 Earth masses of rocky material into the convection zone of HIP 68468 by blue triangles. The best fit is provided with a mix of two and four Earth masses of meteoritic-like and Earth-like material, respectively.

The same amount of rocky material (6 Earth masses) is more than enough to explain its Li enhancement. The net lithium enhancement is hard to predict because it depends on (i) the initial stellar lithium content at the time of accretion; (ii) the stellar Li depletion since the planet accretion; (iii) the efficiency of thermohaline instabilities for depletion of Li that is due to the planet engulfment (Théado & Vauclair 2012). For example, if there is no extra depletion that is due to thermohaline mixing, then we find that the planet accretion event could have occurred when the star had A(Li) $\sim$ 2 dex, corresponding to an age of about 1 Gyr. Assuming that thermohaline mixing depletes lithium by 0.5 dex or 1.0 dex, then the initial Li at the time of planet accretion was either 1.45 dex or 0.9 dex, corresponding to ages of about 3 or 6 Gyr, respectively. This means that if thermohaline mixing is very efficient, depleting Li in about 1 dex, then the planet accretion event occurred recently.

If accretion of planetary material occurred in recent times, then debris may remain around the star. The low $\log(R'_{HK})$ activity index of HIP 68468, while not obviously anomalous for its age group, might in part be due to absorption by dust in the chromospheric Ca II lines similar to the effect seen in WASP-12 (Haswell et al. 2012; Fossati et al. 2013). Further observations including photometric monitoring for anomalously shaped transits of dust clouds would test this hypothesis. Although the activity index might be affected by the dust, the stellar activity as traced by the RVs would not. The low RV jitter is therefore consistent with the old age and low $\log(R'_{HK})$.

Meléndez et al. (2009) and Ramírez et al. (2009) argued that the Sun is deficient in refractory elements relative to the majority solar twins, probably because of the formation of terrestrial planets in the solar system. Most solar twins are therefore enhanced in refractory elements relative to the Sun, such as the solar twin HIP 68468. However, it must be stressed that the refractory enhancement of most solar twins may be primordial, unlike the case of HIP 68468, where the refractory enrichment seems to be due to planet accretion at least 1 Gyr after the star was born. This distinction can be made thanks to the enhanced lithium in HIP 68468, in contrast to most solar twins, which follow a well-defined Li-age correlation.

5. Concluding remarks

We have discovered two strong planet candidates, a close-in (0.66 AU) planet more massive than Neptune and a close-in (0.03 AU) super-Earth, around the solar twin HIP 68468. We have recently been granted *Spitzer* time to search for the transit of this super-Earth.

The host star has enhanced abundances of refractory elements relative to the Sun. After corrections for GCE to bring the [X/H] abundance ratios to the solar age, the correlation with condensation temperature is even stronger, and the element-to-element scatter about the fit with T_{cond} is reduced. The lithium content of HIP 68468 is four times higher than expected for its age. The enhancement of Li and of the refractories can be reproduced by engulfment of a rocky planet with 6 Earth masses.

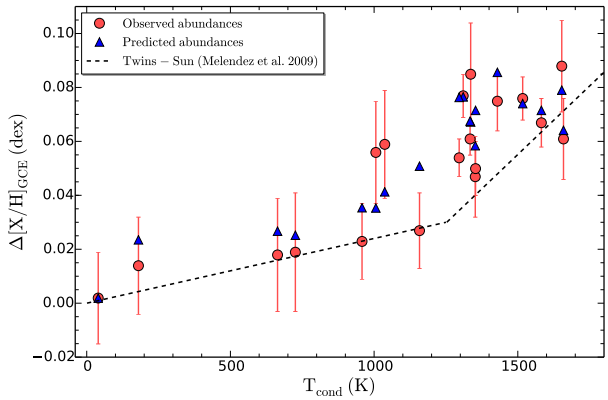

Fig. 10. Observed abundance ratios $[X/H]_{GCE}$ in HIP 68468 as a function of condensation temperature (red circles). The abundances are corrected for galactic chemical evolution to the Sun's age. Planet engulfment of 6 Earth masses of rocky material (blue triangles) can explain the enhancement of refractory elements. The mean abundance trend of 11 solar twins relative to the Sun (Meléndez et al. 2009) is shown by the dashed line.

The planet configuration of HIP 68468 suggests planet migration, which might have resulted in planet accretion events that left signatures on the chemical composition of the host star, as observed for HIP 68468, and in agreement with the predictions by Sandquist et al. (2002).

The recent discoveries of stars showing chemical anomalies possibly related to planet engulfment episodes (Ashwell et al. 2005; Spina et al. 2015) and the exciting case of HIP 68468 open the possibility to extend the search to other objects with such distinctive chemical patterns. Identifying a population of such objects will provide important indications of dynamical interactions of planets and the mechanisms that can drive the evolution of systems similar to our own.

While the detection of the two planets is formally statistically significant (see Sect. 2.3), secure detection of small planets with the radial velocity technique has typically been based on a substantially larger number of measurements given the challenges of stellar activity and reliable period determination with sparse sampling (e.g. Pepe et al. 2011). The intriguing evidence of planet accretion in the form of the enhanced refractory element and lithium abundances warrants further observations to verify the existence of the planets that are indicated by our data and to better constrain the nature of the planetary system around this unique star.

Acknowledgements. We would like to thank the many scientists and engineers who made HARPS possible. Thanks also to Carole Haswell and Dan Staab for useful discussion. J.M. acknowledges support from FAPESP (2012/24392-2) and CNPq (Bolsa de Produtividade). M.B. is supported by the National Science Foundation (NSF) Graduate Research Fellowships Program (grant no. DGE-1144082). J.B. and M.B. acknowledge support for this work from the NSF (grant no. AST-1313119). J.B. is also supported by the Alfred P. Sloan Foundation and the David and Lucile Packard Foundation. M.A. acknowledges support from the Australian Research Council (grants FL110100012 and DP120100991).

References

Anstee, S. D., & O'Mara, B. J. 1995, MNRAS, 276, 859

Asplund, M., Grevesse, N., Sauval, A. J., Allende Prieto, C., & Blomme, R. 2005, A&A, 431, 693
Asplund, M., Grevesse, N., Sauval, A. J., & Scott, P. 2009, ARA&A, 47, 481
Ashwell, J. F., Jeffries, R. D., Smalley, B., et al. 2005, MNRAS, 363, L81
Barklem, P. S., & O'Mara, B. J. 1997, MNRAS, 290, 102
Barklem, P. S., O'Mara, B. J., & Ross, J. E. 1998, MNRAS, 296, 1057
Barklem, P. S., Belyaev, A. K., Spielfiedel, A., Guitou, M., & Feautrier, N. 2012, A&A, 541, A80
Baumann, P., Ramírez, I., Meléndez, J., Asplund, M., & Lind, K. 2010, A&A, 519, A87
Bedell, M., Meléndez, J., Bean, J. L., et al. 2014, ApJ, 795, 23
Bedell, M., Meléndez, J., Bean, J. L., et al. 2015, A&A, 581, A34
Bernstein, R., Shectman, S. A., Gunnels, S. M., Mochnacki, S., & Athey, A. E. 2003, Proc. SPIE, 4841, 1694
Butler, R. P., & Marcy, G. W. 1996, ApJ, 464, L153
Butler, K., Mendoza, C., & Zeippen, C. J. 1993, J. Phys. B, 26, 4409
Carlos, M., Nissen, P. E., & Meléndez, J. 2016, A&A, 587, A100
Castelli, F., & Kurucz, R. L. 2004, ArXiv e-prints [arXiv:astro-ph/0405087]
Castro, M., Do Nascimento, J. D., Jr., Biazzo, K., Meléndez, J., & de Medeiros, J. R. 2011, A&A, 526, A17
Chambers, J. E. 2010, ApJ, 724, 92
Charbonnel, C., & Talon, S. 2005, Science, 309, 2189
Cox, A. N. 2000, Allen's Astrophysical Quantities (New York: AIP Press; Springer)
Cunto, W., & Mendoza, C. 1992, Rev. Mexicana Astron. Astrofis., 23, 107
Dawson, R. I., & Fabrycky, D. C. 2010, ApJ, 722, 937
Demarque, P., Woo, J.-H., Kim, Y.-C., & Yi, S. K. 2004, ApJS, 155, 667
Denissenkov, P. A. 2010, ApJ, 719, 28
Do Nascimento, J. D., Jr., Castro, M., Meléndez, J., et al. 2009, A&A, 501, 687
dos Santos, L. A., Meléndez, J., do Nascimento, J.-D., Jr., et al. 2016, A&A, 592, A156
Doyle, A. P., Davies, G. R., Smalley, B., Chaplin, W. J., & Elsworth, Y. 2014, MNRAS, 444, 3592
Dumusque, X., Lovis, C., Ségransan, D., et al. 2011, A&A, 535, A55
Dumusque, X., Boisse, I., & Santos, N. C. 2014, ApJ, 796, 132
Fossati, L., Ayres, T. R., Haswell, C. A., et al. 2013, ApJ, 766, L20
Galarza, J. Y., Meléndez, J., Ramírez, I., et al. 2016a, A&A, 589, A17
Galarza, J. Y., Meléndez, J., & Cohen, J. G. 2016b, A&A, 589, A65
Gelman, A. & Rubin, D. B. 1992, Statist. Sci., 7, 457
Gonzalez, G. 1997, MNRAS, 285, 403
Gray, D. F. 2005, The Observation and Analysis of Stellar Photospheres, 3rd edn. (Cambridge, UK: Cambridge University Press)
Haswell, C. A., Fossati, L., Ayres, T., et al. 2012, ApJ, 760, 79
Høg, E., Fabricius, C., Makarov, V. V., et al. 2000, A&A, 355, L27
Howard, A. W., Johnson, J. A., Marcy, G. W., et al. 2011, ApJ, 726, 73
Kass, E. R., & Raftery, E. A. 1995, J. Amer. Stat. Assoc., 90, 773
Lambert, D. L. 1993, Physica Scripta Volume T, 47, 186
Lind, K., Asplund, M., & Barklem, P. S. 2009, A&A, 503, 541
Lind, K., Asplund, M., Barklem, P. S., & Belyaev, A. K. 2011, A&A, 528, A103
Lo Curto, G., Pepe, F., Avila, G., et al. 2015, The Messenger, 162, 9
Lovis, C., Dumusque, X., Santos, N. C., et al. 2011, ArXiv e-prints [arXiv:1107.5325], unpublished
Mamajek, E. E., & Hillenbrand, L. A. 2008, ApJ, 687, 1264
Mayor, M., & Queloz, D. 1995, Nature, 378, 355
Mayor, M., Pepe, F., Queloz, D., et al. 2003, The Messenger, 114, 20
Marcy, G. W., & Butler, R. P. 1996, ApJ, 464, L147
Meléndez, M., Bautista, M. A., & Badnell, N. R. 2007, A&A, 469, 1203
Meléndez, J., Asplund, M., Gustafsson, B., & Yong, D. 2009, ApJ, 704, L66
Meléndez, J., Bergemann, M., Cohen, J. G., et al. 2012, A&A, 543, A29
Meléndez, J., Ramírez, I., Karakas, A. I., et al. 2014a, ApJ, 791, 14
Meléndez, J., Schirbel, L., Monroe, T. R., et al. 2014b, A&A, 567, L3
Monroe, T. R., Meléndez, J., Ramírez, I., et al. 2013, ApJ, 774, L32
Montalbán, J., & Rebolo, R. 2002, A&A, 386, 1039
Murray, N., & Chaboyer, B. 2002, ApJ, 566, 442
Nissen, P. E. 2015, A&A, 579, A52
Önehag, A., Korn, A., Gustafsson, B., Stempels, E., & Vandenberg, D. A. 2011, A&A, 528, A85
Osorio, Y., Barklem, P. S., Lind, K., et al. 2015, A&A, 579, A53
Pepe, F., Lovis, C., Ségransan, D., et al. 2011, A&A, 534, A58
Ramírez, I., Allende Prieto, C., & Lambert, D. L. 2007, A&A, 465, 271
Ramírez, I., Meléndez, J., & Asplund, M. 2009, A&A, 508, L17
Ramírez, I., Meléndez, J., Cornejo, D., Roederer, I. U., & Fish, J. R. 2011, ApJ, 740, 76
Ramírez, I., Meléndez, J., & Chanamé, J. 2012, ApJ, 757, 164
Ramírez, I., Allende Prieto, C., & Lambert, D. L. 2013, ApJ, 764, 78
Ramírez, I., Meléndez, J., Bean, J., et al. 2014, A&A, 572, A48
Ramírez, I., Khanal, S., Aleo, P., et al. 2015, ApJ, 808, 13
Samson, A. M., & Berrington, K. A. 2001, Atom. Data Nucl. Data Tables, 77, 87
Sandquist, E. L., Dokter, J. J., Lin, D. N. C., & Mardling, R. A. 2002, ApJ, 572, 1012
Santos, N. C., Bouchy, F., Mayor, M., et al. 2004, A&A, 426, L19
Shi, J. R., Gehren, T., Zeng, J. L., Mashonkina, L., & Zhao, G. 2014, ApJ, 782, 80
Siess, L., Dufour, E., & Forestini, M. 2000, A&A, 358, 593
Sneden, C. A. 1973, Ph.D. Thesis, The University of Texas at Austin, USA
Spina, L., Palla, F., Randich, S., et al. 2015, A&A, 582, L6
Spina, L., Meléndez, J., & Ramírez, I. 2016, A&A, 585, A152
Teske, J. K., Khanal, S., & Ramírez, I. 2016, ApJ, 819, 19
Théado, S., & Vauclair, S. 2012, ApJ, 744, 123
Tognelli, E., Prada Moroni, P. G., & Degl'Innocenti, S. 2016, MNRAS, 460, 3888
Tucci Maia, M., Meléndez, J., & Ramírez, I. 2014, ApJ, 790, L25
Tucci Maia, M., Ramírez, I., Meléndez, J., et al. 2016, A&A, 590, A32
Xiong, D. R., & Deng, L. 2009, MNRAS, 395, 2013
Yan, H. L., Shi, J. R., & Zhao, G. 2015, ApJ, 802, 36
Zakamska, N. L., Pan, M., & Ford, E. B. 2011, MNRAS, 410, 1895
Zatsarinny, O., Bartschat, K., Gedeon, S., et al. 2009, Phys. Rev. A, 79, 052709
Zechmeister, M., Kürster, M. 2009, A&A, 496, 577

Appendix A: NLTE corrections for Mg and Ca

Our Mg and Ca atom models for NLTE calculations are unpublished, although our Mg model is somewhat similar to the Mg atom model recently published by Osorio et al. (2015). A brief description of our Mg and Ca models is given below. Radiative data were downloaded from the Kurucz (http://www.pmp.uni-hannover.de/cgi-bin/ssi/test/kurucz/sekur.html) and TOPbase (Cunto & Mendoza 1992) web interfaces in July 2011. When necessary, the atoms were supplemented with hydrogenic data. The TOPbase reference for Mg I is Butler et al. (1993), for Mg II it is "K. T. Taylor, to be published", for CaI and CaII it is "H. E. Saraph & P. J. Storey, to be published". We included 220 energy levels for Mg, complete up to $n = 80$ for Mg I and up to $n = 10$ for Mg II. Fine structure is resolved up to $l \leq 3$ (s, p, d, f) and $n \leq 19$ in Mg I; $n = 20$–80 are collapsed super levels. For Ca we included 256 energy levels, with identical coverage as for Mg. For Mg and Ca, 1390 and 1961 b-b radiative transitions were included, respectively; f-values are taken from TOPbase preferentially, otherwise from the Kurucz database. Collisional broadening due to collisions with neutral H is based on the ABO theory (Anstee & O'Mara 1995; Barklem & O'Mara 1997; Barklem et al. 1998) when possible (~15 lines for each atom). Stark broadening is neglected. Photoionisation cross-sections are from TOPbase for both ionisation stages. Electron excitation and ionisation were taken from Cox (2000). Cross-sections for forbidden transitions were computed assuming $f = 0.5$, and when available replaced with Zatsarinny et al. (2009) for Mg and Samson & Berrington (2001) and Meléndez et al. (2007) for Ca. For hydrogen collisions we adopted Sh = 0.1 (Lambert 1993), and replaced with Barklem et al. (2012) when available for Mg.

Appendix B: Additional tables

Table B.2. HARPS measured radial velocities and activity indices for HIP 68468.

Julian date	RV (km s^{-1})	$\sigma_{\rm RV}$ (km s^{-1})	$S_{\rm HK}$	$\sigma_{S_{\rm HK}}$	$FWHM$ (km s^{-1})
2455983.87576651	1.2544	0.0009	0.1514	0.0006	7.3631
2455984.85786337	1.2525	0.0011	0.1538	0.0008	7.3684
2455985.85166182	1.2531	0.0010	0.1504	0.0007	7.3638
2455986.87231354	1.2534	0.0010	0.1502	0.0007	7.3674
2456042.62854487	1.2545	0.0012	0.1526	0.0009	7.3742
2456046.75246848	1.2524	0.0015	0.1491	0.0011	7.3754
2456047.79316449	1.2523	0.0011	0.1547	0.0008	7.3708
2456048.80623149	1.2520	0.0010	0.1508	0.0008	7.3782
2456300.86637575	1.2571	0.0010	0.1527	0.0008	7.3743
2456301.83524661	1.2588	0.0012	0.1501	0.0009	7.3758
2456375.81375898	1.2526	0.0009	0.1547	0.0007	7.3751
2456376.85878275	1.2577	0.0009	0.1493	0.0007	7.3807
2456377.75584570	1.2518	0.0010	0.1550	0.0008	7.3756
2456378.74306280	1.2529	0.0010	0.1557	0.0008	7.3669
2456379.77212101	1.2500	0.0010	0.1531	0.0008	7.3723
2456380.77432459	1.2533	0.0009	0.1541	0.0007	7.3763
2456381.77268400	1.2538	0.0008	0.1546	0.0007	7.3736
2456484.55514629	1.2572	0.0010	0.1507	0.0008	7.3752
2456485.56989639	1.2592	0.0010	0.1541	0.0008	7.3797
2456487.56527760	1.2576	0.0009	0.1577	0.0007	7.3759
2456488.54822341	1.2590	0.0010	0.1502	0.0007	7.3806
2456489.53769598	1.2570	0.0011	0.1527	0.0009	7.3827
2456708.80804387	1.2569	0.0011	0.1514	0.0008	7.3740
2456709.82927988	1.2542	0.0014	0.1492	0.0010	7.3770
2456710.82693680	1.2588	0.0012	0.1527	0.0010	7.3747
2456711.80101463	1.2571	0.0013	0.1527	0.0010	7.3711
2456850.53875184	1.2570	0.0014	0.1418	0.0010	7.3771
2456851.59721308	1.2559	0.0015	0.1478	0.0011	7.3842
2456852.57164175	1.2564	0.0014	0.1550	0.0010	7.3805
2456855.58294963	1.2577	0.0013	0.1457	0.0009	7.3857
2456856.55065259	1.2584	0.0010	0.1536	0.0008	7.3762
2457025.79937601	1.2556	0.0013	0.1503	0.0010	7.3805
2457025.85879076	1.2542	0.0011	0.1558	0.0009	7.3854
2457026.86222108	1.2540	0.0010	0.1543	0.0008	7.3705
2457028.85867790	1.2558	0.0012	0.1536	0.0009	7.3814
2457226.56087032	1.2673	0.0011	0.1509	0.0009	7.3994
2457227.53935745	1.2735	0.0009	0.1480	0.0008	7.3972
2457228.50134125	1.2696	0.0009	0.1474	0.0007	7.3925
2457228.58842818	1.2675	0.0011	0.1505	0.0009	7.3977
2457229.48290638	1.2735	0.0008	0.1503	0.0006	7.3945
2457230.49026756	1.2712	0.0009	0.1491	0.0007	7.3909
2457230.61575371	1.2699	0.0011	0.1464	0.0009	7.3941
2457232.51912010	1.2712	0.0018	0.1489	0.0013	7.3962
2457511.82148708	1.2733	0.0009	0.1509	0.0008	7.4031
2457587.57535340	1.2727	0.0013	0.1477	0.0010	7.3964

Table B.1. Differential abundances of HIP 68468 relative to the Sun and errors.

Element	[X/H]	$\Delta T_{\rm eff}$ +8 K	$\Delta\log g$ +0.02 dex	$\Delta v_{\rm t}$ +0.01 km s^{-1}	Δ[Fe/H] +0.01 dex	Param[a]	Obs[b]	Total[c]
	(dex)	(dex)	(dex)	(dex)	(dex)	(dex)	(dex)	(dex)
Li	1.52[d]	0.01	0.00	0.00	0.00	0.01	0.03	0.03
C	0.043	–0.005	0.005	0.000	0.000	0.007	0.012	0.014
CH	0.027	0.006	–0.001	0.000	0.007	0.009	0.026	0.028
C_2	0.050	0.007	0.001	0.000	0.007	0.010	0.005	0.011
O	0.055	–0.008	0.003	–0.001	0.002	0.009	0.005	0.010
Na	0.065	0.003	–0.001	0.000	0.000	0.003	0.002	0.006
Mg	0.105	0.006	–0.002	–0.003	0.000	0.007	0.017	0.018
Al	0.115	0.003	–0.002	–0.001	0.000	0.004	0.015	0.015
Si	0.093	0.001	0.001	–0.001	0.001	0.002	0.006	0.006
S	0.047	–0.004	0.005	0.000	0.001	0.006	0.017	0.018
K	0.094	0.006	–0.008	–0.002	0.001	0.010	0.009	0.014
Ca	0.070	0.005	–0.003	–0.002	0.000	0.006	0.003	0.007
Sc I	0.093	0.006	0.000	0.000	–0.001	0.006	0.009	0.011
Sc II	0.104	0.000	0.007	–0.002	0.003	0.008	0.006	0.010
Ti I	0.082	0.007	0.000	–0.002	–0.001	0.007	0.006	0.009
Ti II	0.086	0.000	0.007	–0.002	0.003	0.008	0.011	0.014
V	0.089	0.008	0.000	–0.001	–0.001	0.008	0.005	0.010
Cr I	0.057	0.006	–0.001	–0.002	0.000	0.006	0.006	0.009
Cr II	0.048	–0.003	0.007	–0.002	0.002	0.008	0.008	0.011
Mn	0.055	0.006	–0.002	–0.003	0.000	0.007	0.008	0.011
Fe I	0.065	0.006	–0.001	–0.002	0.000	0.006	0.002	0.007
Fe II	0.064	–0.002	0.007	–0.003	0.003	0.008	0.004	0.009
Co	0.082	0.006	0.002	0.000	0.000	0.006	0.008	0.010
Ni	0.079	0.005	0.000	–0.002	0.000	0.005	0.003	0.006
Cu	0.105	0.004	0.001	–0.001	0.001	0.004	0.013	0.014
Zn	0.056	0.000	0.001	–0.003	0.002	0.004	0.018	0.018

Notes. Abundances of V, Mn, Co, and Cu accounted for HFS. NLTE effects were considered for Li, O, Na, Mg, Ca, and Cu; LTE abundances for these elements are 1.48, 0.083, 0.069, 0.099, 0.075, 0.105 dex, respectively. [(a)] Adding errors in stellar parameters. [(b)] Observational errors. [(c)] Total error (stellar parameters and observational). [(d)] A(Li) is reported rather than [Li/H].